Dynamic flood topographies in the Terai region of Nepal

E.H. Dingle[1,2], M. Creed[2], H.D. Sinclair[2], D. Gautam[3], N. Gourmelen[2], A.G.L. Borthwick[4], M. Attal[2]

[1]*Department of Geography, Simon Fraser University, Burnaby, BC, Canada*

[2]*School of GeoSciences, University of Edinburgh, Drummond Street, Edinburgh, EH8 9XP, UK*

[3]*Practical Action Consulting, Kathmandu 15135, Nepal*

[4]*School of Engineering, University of Edinburgh, King's Buildings, Edinburgh, EH9 3FB, UK*

Keywords: Nepal, flood inundation, channel mobility, bifurcation, Delft3D

Abstract

Flood hazard maps used to inform and build resilience in remote communities in the Terai region of southern Nepal are based on outdated and static digital elevation models (DEMs), which do not reflect dynamic river configuration or hydrology. Episodic changes in river course, sediment dynamics, and the distribution of flow down large bifurcation nodes can modify the extent of flooding in this region, but these processes are rarely considered in flood hazard assessment. Here, we develop a 2D hydrodynamic flood model of the Karnali River in the Terai region of west Nepal. A number of scenarios are tested examining different DEMs, variable bed elevations to simulate bed aggradation and incision, and updating bed elevations at a large bifurcation node to reflect field observations. By changing the age of the DEM used in the model, a 9.5% increase in inundation extent was

22 observed for a 20-year flood discharge. Reducing horizontal DEM resolution alone,
23 resulted in a <1% change in inundation extent. Uniformly varying the bed elevation
24 between model runs to simulate the effect of sediment deposition or incision led to a 36%
25 change in inundation extent. Finally, changes in bed elevation at the main bifurcation node
26 to reflect observed conditions in the Karnali River resulted in a 32% change in modelled
27 flood inundation extent. Our results suggest that regular field measurements of bed
28 elevation and updated DEMs following large sediment generating events and at
29 topographically sensitive areas, such as large river bifurcations, could help improve model
30 inputs in future flood prediction models. This is particularly important following large flood
31 events carrying large sediment loads out of mountainous regions that could promote bed
32 aggradation and channel switching across densely populated alluvial river systems and
33 floodplains further downstream.

34

35 ## 1. Introduction

36 Rivers sourced from the Himalayan mountains irrigate the Indo-Gangetic Plain and support
37 about 10% of the global population. Many of these rivers are also the source of devastating
38 floods, with effects further compounded where isolated communities, living on the river
39 floodplain, lack disaster risk management and resilience measures. In Nepal alone, flood
40 disasters were responsible for over US$130 million losses and nearly one third of all natural
41 disaster-related deaths between 2001 and 2008 (Risk Nexus, 2015). Specific examples
42 include the 2008 Kosi River avulsion (e.g. Sinha, 2009; Chakraborty et al., 2010), and the
43 2013 Uttarakhand floods that killed over 5,000 people and are viewed as India's worst

44 natural disaster since 2004 (e.g. Rana et al., 2013). While early warning systems saved
45 many lives in the 2014 Karnali River floods, which impacted 120,000 people living in the
46 Terai region in western Nepal, gaps in the disaster management system were still
47 apparent. Water levels rose to around 16 m at Chisapani (where the river exits the
48 mountain front and enters the Indo-Gangetic Plain), 1 m higher than the previous record in
49 1983; the return interval for this 2014 event was estimated to be 1000 years (Risk Nexus,
50 2015). In the post-event review capability report produced in the aftermath of the flood
51 (Risk Nexus, 2015), stakeholders highlighted that flood risk is currently underestimated, a
52 potential cause being that changes to the channel bed are not included in flood risk
53 assessments. Where sediment deposition within channels reduces channel capacity,
54 specific event discharges (e.g. the 20-year flood discharge of ~17,000 m^3/s) are likely to
55 have increased inundation extent because channel capacity will be exceeded earlier in the
56 rising limb of the flood hydrograph, and remain over bank for longer (Stover and
57 Montgomery, 2001; Lane et al., 2007, Slater et al., 2015). Flood hazard may also be
58 incorrectly estimated in other similar major river systems downstream of the Himalayan
59 mountains across the Indo-Gangetic Plain, many of which are largely aggradational in
60 nature, with high rates of channel avulsion (see e.g. Sinha et al., 2009).

61 Changes in river course and sediment dynamics that alter the morphology (e.g.
62 channel geometry and form) of river channels and adjacent floodplain have been shown to
63 modify the likelihood of flooding (e.g. Stover and Montgomery, 2001; Lane et al., 2007;
64 Slater et al., 2015; Slater et al., 2019), yet these processes are rarely considered in flood
65 hazard assessment. Flood inundation extent is primarily determined by flow discharge, in
66 particular the magnitude of peak flow. But, for a given flow, the extent to which water levels

overtop the local bank and flow out onto the adjacent floodplain is also controlled by channel conveyance (Lane et al., 2007). River systems downstream of the Himalayan mountain front are typically described as shallow, aggrading alluvial systems (e.g. Sinha et al., 2005; Tandon et al., 2006; Dingle et al., 2016) which are characterised by large sediment loads (Sinha and Friend, 1994; Lupker et al., 2012) and high rates of lateral channel migration and avulsion (Chakraborty et al., 2010; Dingle et al., 2020). Sediment accumulation in channels may be caused by simple natural variability in sediment flux from upstream parts of the catchment, but also by changes in land-use, engineering works (e.g. damming), climate change (e.g. increased rainfall intensity) and landslides (e.g. resulting from intense monsoon and/or earthquake). This can result in alluvial channels with fluctuating bed elevations (and therefore channel conveyance) if sediment is not immediately evacuated, which may modify flood inundation extent during subsequent high flow discharges. Understanding both hydrological processes and sediment dynamics are key to mitigating flood risk in aggrading, low relief landscapes characterised by rivers with high sediment supply (e.g. Aalto et al., 2003). Flood hazard maps used to inform communities downstream of the Himalayan mountains and build resilience to these types of events are based upon static and outdated Digital Elevation Models (DEMs), which do not reflect the dynamic river configuration or hydrology (Risk Nexus, 2015).

Here, we use a new Delft3D flood inundation model that incorporates field geomorphological evidence (e.g. measured channel geometry and bed elevations) and a high resolution DEM of the landscape that more closely reflects the current configuration of the Karnali River in west Nepal (Figure 1). The first aim of this paper is to examine the change in flood inundation extent resulting from a change in model and DEM. The new 2D

hydrodynamic model is tested for several flood scenarios and the results compared against existing modelled predictions generated using a different hydrological model (1D HEC-RAS, undertaken by the Nepal Department of Hydrology and Meteorology – DHM). The effect of changing the DEM is examined in terms of improved spatial resolution and the difference in channel configuration between the two DEMs (that were captured more than 10 years apart). The second aim is to test how modelled flood inundation extent responds to varying channel bed elevation, to simulate bed aggradation and incision that might be expected following delivery of sediment pulses into the foreland basin. The final aim of the paper is to assess the sensitivity of flow routing and flood inundation extent, downstream of a major bifurcation node, to changes in bed elevation. We do this through updating bed elevations at a large bifurcation node on the Karnali River to reflect field observations, and compare the modelled results to observed discharge ratios between the two branches. The results demonstrate the sensitivity of model predictions of fluvial inundation to the horizontal and vertical resolution of the DEM. This is particularly relevant in the low gradient setting of the Terai. Additionally, we show that changes in bed elevation, typical of changes induced by increased sediment supply from the mountain catchment, drive flood inundation into areas that were previously unaffected.

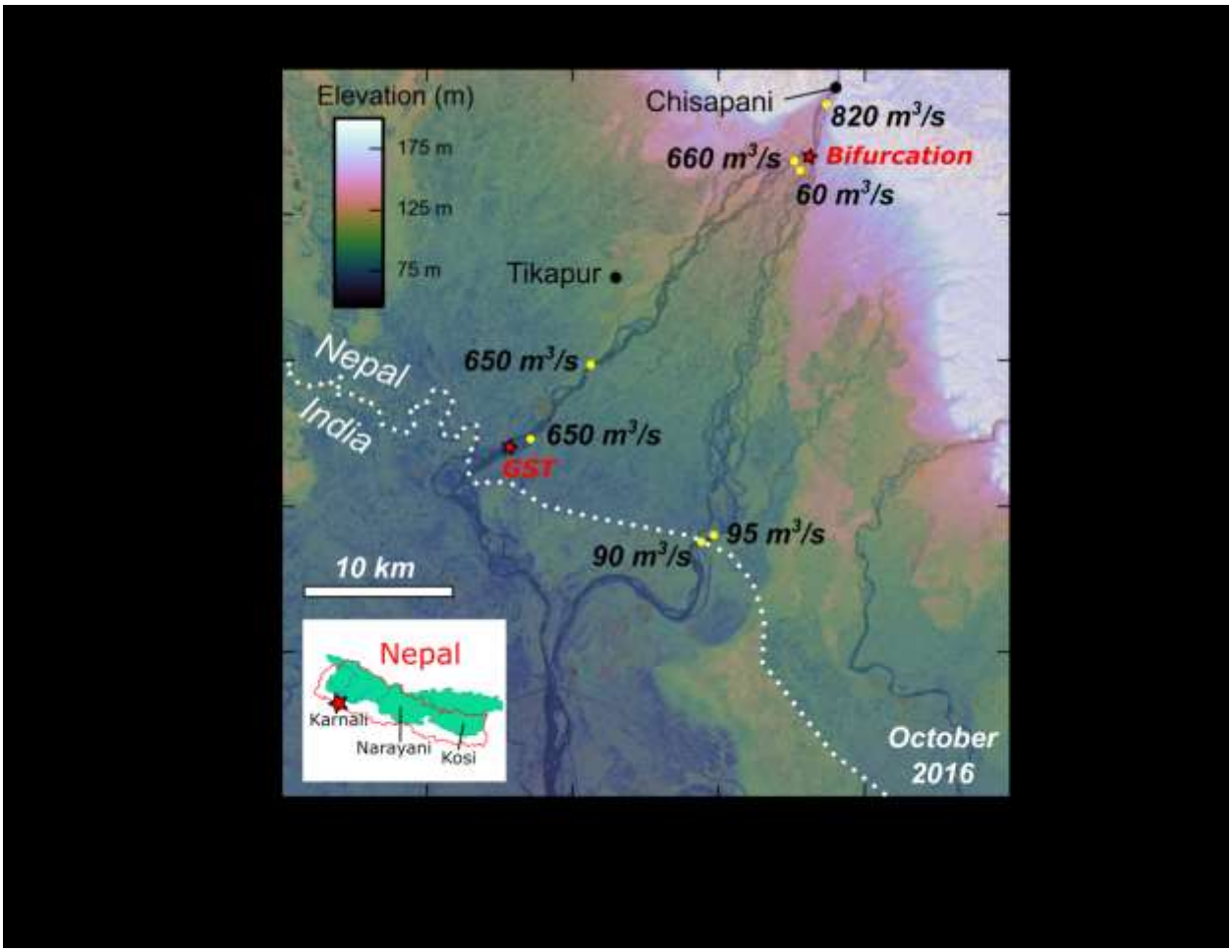

107

108 *Figure 1 - Karnali River downstream of Chisapani. The positions of the bifurcation and gravel-sand transition*
109 *(GST) are shown by red stars. Average discharge measurements from Acoustic Doppler Current Profiler*
110 *(ADCP) surveys on the Karnali River in October 2016 are also shown (yellow circles). Of the ~820 m^3/s*
111 *recorded at Chisapani, ~80-90% of flow is directed into the west branch of the river at the bifurcation. ADCP*
112 *surveys at the bifurcation point did not capture the entirety of flow directed into the east branch, as there was*
113 *an additional channel further east which was not accessible. Based on the discharge measurements made*
114 *on the east branch further downstream (90-95 m^3/s), this small channel was likely to only be conveying ~30*
115 *m^3/s. The ~100 m^3/s lost between the upstream sample (820 m^3/s) and bifurcation point may also be due to*
116 *water diversion into the canal network immediately downstream of the Chisapani bridge, to flow into small*
117 *braid channels in the floodplain, and to underground flow through the thick porous sediment (which is absent*
118 *at the most upstream site where the channel is bedrock). Data sources: 30 m Shuttle Radar Topography*

Mission (SRTM) Digital Elevation Model (coordinates in UTM Zone 43N) and Sentinel-2 optical satellite imagery (captured October 26, 2016).

2. Methods

2.1 *Geomorphological setting*

The Karnali basin has a drainage area of ~43,000 km^2 upstream of the mountain outlet at the town of Chisapani (Figure 1), where the channel exits a confined bedrock gorge and flows out onto the alluvial Indo-Gangetic Plain. In the upper reaches of the alluvial plain, the channel is characterized by a coarse gravel to cobble bed which fines downstream (D_{50} = 46-148 mm between the mountain front and gravel-sand transition; Quick et al., 2019). The gravel channel is braided with exposed gravel bars (at low flow) and mature, vegetated islands. At ~5 km downstream, the channel bifurcates into two branches. The gradient of the gravel reaches, which extend to the gravel-sand transition at ~40 km downstream in each branch, is 0.001-0.002 m/m (Dingle et al., 2020). The gravel-sand transition occurs over a distance of ~2-3 km, downstream of which the channel bed is exclusively sand, and the two branches of the Karnali River rejoin. The channels are considerably more mobile in the sand-bed portion of the river system and can migrate hundreds of meters in a single year (Dingle et al., 2020). The average gradient of the sand channel is approximately half that of the gravel reach.

The flow is seasonal, and dominated by the Indian Summer Monsoon. Since 1962, when the gauging station at Chisapani was installed, the average daily discharge recorded

140 from November to April ranges from 400 m^3/s to 600 m^3/s, but can be as low as 200 m^3/s.
141 The peak monsoon flood has been observed as early as June and as late as October, and
142 peak flood usually arrives in August. From the gauging station records, peak flood
143 discharges exceed 5,000 m^3/s annually. The maximum instantaneous discharge since
144 1962 was recorded on August 15th, 2014, estimated as ~ 22,000 m^3/s.
145

146 *2.2 Digital Elevation Model (DEM)*

147 TanDEM-X imagery was used to generate Digital Elevation Models of the channel system.
148 TerraSAR-X has a repeat period of 11 days, and data acquired by both satellites, flying in
149 tandem, have a spatial resolution on the order of 1 m (Krieger et al., 2007; Eineder et al.,
150 2011) thereby providing excellent temporal and spatial resolution for observing topography
151 and how it changes. The radar platforms enabled us to use imagery acquired in non-
152 daylight hours and cloudy conditions, in contrast to optical platforms. We derived a 10 m
153 resolution DEM dated 23rd February 2013 from conventional SAR interferometric
154 processing of bi-static TanDEM-X imagery (Dehecq et al., 2016). A Shuttle Radar
155 Topography Mission (SRTM) DEM was used as a reference during the unwrapping stage
156 to minimize unwrapping errors.

157 No-data values in the 2013 TanDEM-X DEM (10 m spatial resolution) were filled
158 with data from a 30 m resolution SRTM DEM (captured in 2000). In general, no-data
159 regions corresponded with the wet portion of the river channel. In the regions that were too
160 large to interpolate elevations between opposite banks, pixels in the 30 m SRTM DEM
161 were resampled to the same resolution as the TanDEM-X DEM (10 m) prior to filling.
162 Topographic noise was then suppressed across the entire DEM using a Wiener filter

(Pelletier, 2013; Grieve et al., 2016). The large vertical error associated with the SRTM data used to patch the no-data values in the TanDEM-X data resulted in large artificial jumps in the elevation of the channel bed (10 - 20 m changes in elevation between adjacent pixels) despite the Wiener filtering. This may in part be due to the shift in channel position between the times that the two DEMs were captured. In order to correct for this, the region of the DEM which corresponded to the active channel was smoothed using a focal mean smoothing radius of 3 x 3 pixels. This was repeated until the area of the DEM representing the active channel was effectively free of artificial highs and lows. Given the exceptionally low gradient and relief of the Karnali channel and its adjacent floodplain, this method generated a reasonable representation of topographic conditions across the study area.

The vertical error or root-mean-square error (RMSE) associated with the SRTM DEM elevations can vary between ±6.2 and ±22.35 m depending on vegetation cover (Carabajal and Harding, 2006; Rodriguez et al., 2006; Wendi et al., 2016). The RMSE of the TanDEM-X DEM is ±1.1 to ±1.8 m (Wessel et al., 2018).

2.3 Field measurements and data collection

Measurements of channel bed elevation and floodplain (bank top) elevation were made in October 2016 using an RTK-GPS system, resolving to cm vertical accuracy. For land surface elevations, a number of RTK-GPS surveys were carried out while absolute channel bed elevations were measured using the same GPS system mounted to a Sontek R9 Acoustic Doppler Current Profiler (ADCP) (Figure 2). Channel transects were surveyed at seven locations using the ADCP to estimate water discharge at Chisapani (upstream of

the bifurcation) and at locations down the west and east branches to ascertain the proportion of flow diverted down each branch (Figure 1). The bank surveys provided information on bankfull channel depth when combined with ADCP data. The elevations of the channel bed down each branch at the bifurcation were surveyed in particular detail because the bed elevations at this location control the ratio of flow diverted down each branch in the Delft3D model.

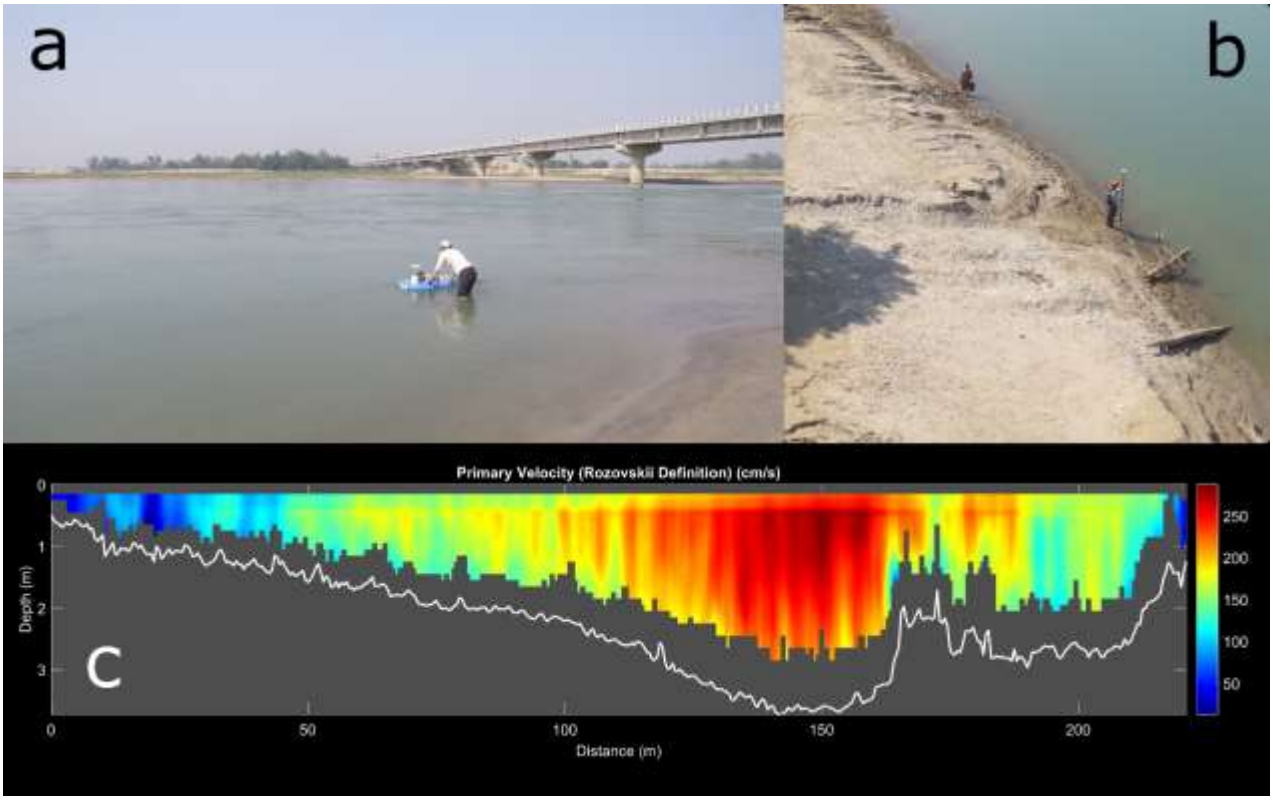

Figure 2. Field surveys carried out on the Karnali River in October 2016. a) Channel geometry and discharge were measured using an Acoustic Doppler Current Profiler (ADCP) at locations shown in Figure 1. b) Absolute bank elevations were determined using an RTK-GPS system to complement the ADCP surveys. c) Example of the ADCP data output using the Velocity Mapping Toolbox (VMT) v4.09 (Parsons et al., 2013) showing cross-section channel geometry and primary flow velocity in cm/s in the downstream direction.

198

199 ## 2.4 Model setup

200 Delft3D was used to create a 2D depth-averaged hydrodynamic model of the Karnali river
201 system, where vertical accelerations were neglected and hydrostatic pressure assumed.
202 The model domain was defined on an orthogonal, curvilinear, structured mesh, with 56,744
203 grid cells (Figure 3). The number of cells was chosen to ensure grid convergence in the
204 most important areas of the domain for the study, including the main river channel and
205 sensitive, flood-prone regions. Grid cell length ranged from 15 to 50 m inside the river, and
206 increased up to 1000 m at the east and west domain boundaries, where no flow was
207 expected, even in extreme flood events. The grid aspect ratio, which determines the
208 smoothness of the flow in the model from cell to cell, ranged from 1.4 to 2.2 within the river
209 and flood-sensitive areas, and up to 2.5 at the outer domain grid cells. For the purpose of
210 the present study, which investigates the effect that DEM age and resolution have on flood
211 inundation maps, sediment transport was not included in the numerical model.

212 The boundaries of the east and west river channels were obtained from the 30 m
213 SRTM DEM. The grid was generated inside the main channels, and then expanded out to
214 the east and west domain boundaries. The downstream boundary is defined where the two
215 branches of the river reconnect, on the Indian side of the Nepal-India border (Figure 1).
216 The upstream boundary is located at the river gauging station in the town of Chisapani,
217 where discharge measurements are recorded regularly.

218 A time-series hydrograph of the discharge was specified at the upstream boundary,
219 located at the Chisapani gauging station, where daily measurements, between 1962 and

2010, were obtained from the Nepal Department of Hydrology and Meteorology (DHM) records. In the absence of discharge or water level data at the downstream boundary, a transmissive boundary condition was specified at the outlet of the domain. The transmissive condition defines the gradient of the water surface, estimated as the gradient of the bathymetry, 0.0001 in this case.

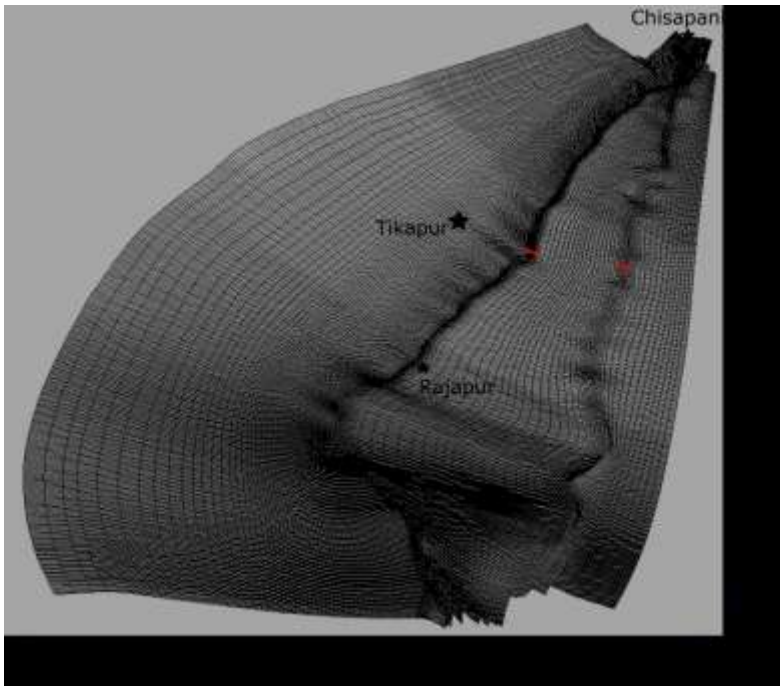

Figure 3. Delft 3D model dimensions and structured mesh. River cross-section locations for evaluating discharge down the east and west branches are shown in red. The largest municipalities, Tikapur, Rajapur and Chisapani, are represented by black stars.

The river channel was filled with water initially, with the same water depth assigned everywhere in the river. Average daily discharge measurements recorded at Chisapani gauging station were used as the input discharge for the model. The 20-year flood, an event that has a 1 in 20 chance of exceedance each year, was modelled in all of the scenarios considered. The discharge of the 20-year flood is ~17,000 m^3/s, estimated by fitting the maximum annual instantaneous discharge measurements from 1962 to 2014 to

a Gumbel distribution (see supplementary data file). A flood of this magnitude was recorded at Chisapani in June 2013. Daily discharge measurements from February to June 2013 (hydrograph available in supplementary material) were used as model input, allowing sufficient time for the model to reach equilibrium prior to the peak flood.

To investigate how the DEM resolution and the type of model used can affect model output, the 20-year flood model was run using TanDEM-X and 30 m SRTM elevation data. The 20-year flood model outputs compared were from: (1) an existing 1D HEC-RAS model, (obtained from the DHM) using the SRTM DEM as the base topographic data (Figure 4a); (2) the Delft3D model using the same SRTM DEM base data (Figure 4b); (3) the Delft3D model using the new 10 m TanDEM-X data as base topographic data (Figure 4c; Table 1); and (4) the Delft3D model using the TanDEM-X data resampled to 30 m, as base topographic data (Figure 4d). In these instances, the river bed elevation was taken from the DEM directly. It is assumed that model configurations and subsequent scenarios run using unmodified DEMs do not account for channel bathymetry, and instead the elevation within the channel boundary is effectively the elevation of the water surface.

Using the results from the Delft3D model with unmodified 10 m TanDEM-X data as a baseline scenario (Scenario 1), the following scenarios were investigated using the Delft3D model and the same hydrological inputs (20-year flood discharge):

Scenario 1 (baseline)

River bed elevation obtained from the TanDEM-X DEM directly, where the channel elevation represents the water surface.

257

258 *Scenario 2 (uniformly lowered bed)*

259 Sampled flow depths surveyed in October 2016 at a number of locations (e.g. Figure 1 and
260 2), were on average 1.5 – 2 m. The surface of the DEM within the channel boundaries was
261 uniformly lowered by 1.8 m across the main channel, approximating field observations.

262

263 *Scenario 3 (bifurcation modification)*

264 This scenario is an extension of Scenario 2. In October 2016, at the bifurcation, bed
265 elevations measured from ADCP surveys were up to 5 m lower than the DEM values in the
266 west branch and 0.5 - 1 m lower in the east branch. In this scenario, as in Scenario 2, the
267 river bed elevation was first uniformly reduced by 1.8 m everywhere within the main river
268 channel. The bed elevations at the bifurcation were then further adjusted to reflect the field
269 observations recorded in October 2016. At the bifurcation, the west branch river bed was
270 reduced further, by up to 3.2 m (to a total of up to 5 m depth), and 0.8 m to 1.3 m was
271 added back to the river bed elevations in the east branch (to generate a total channel depth
272 of 0.5 – 1 m). Changes to the DEM were made on a cell-by-cell basis over a downstream
273 distance of 1 – 2 km to maintain the bed slope and avoid generating artificial discontinuities
274 in the bed.

275

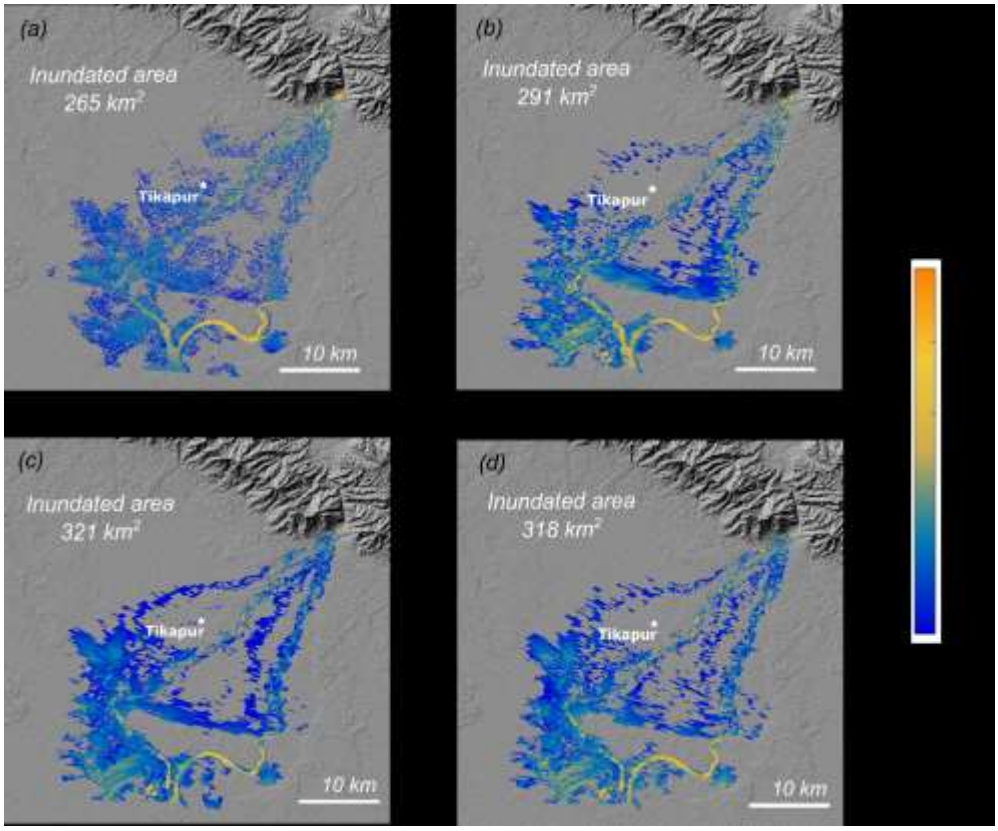

Figure 4. Inundation extent and water depth (> 0.5 m) for a 1 in 20 yr flood discharge for a) the existing HEC-RAS hydrodynamic model and SRTM DEM (inundated area 265 km^2), b) using the new Delft3D model and SRTM DEM (inundated area 291 km^2), c) for Scenario 1 using the Delft3D model and new 10 m TanDEM-X DEM (inundated area 321 km^2), and d) for Scenario 1 using the Delft3D model and 30 m resampled TanDEM-X DEM (inundated area 318 km^2). The same model configurations are presented showing inundation depths >0.05 m in the Supplementary Material.

3. Results

3.1 Field measurements

ADCP transects surveyed in October 2016 revealed a large asymmetry in the distribution of flow between the two branches of the Karnali River downstream of the bifurcation. From

288 the 820 m^3/s discharge measured at the exit of the bedrock canyon at Chisapani, ~80% of
289 the flow was diverted into the west branch and only ~7% of flow was diverted into the east
290 branch (Figure 1). The remaining 'missing' ~13% is likely due to a combination of: capture
291 in smaller braid channels on the west and east branches (which were not surveyed due to
292 access issues), diversion into a canal intake just downstream of the Chisapani transect,
293 and underground flow through the porous alluvium. Transects taken on the west and east
294 branches immediately downstream of the bifurcation revealed that the absolute bed
295 elevation of the channel was ~2 m lower in the west (main) branch, and that flow at the
296 time of survey was ~3.5 m deeper in the west branch than the east (Figure 5).

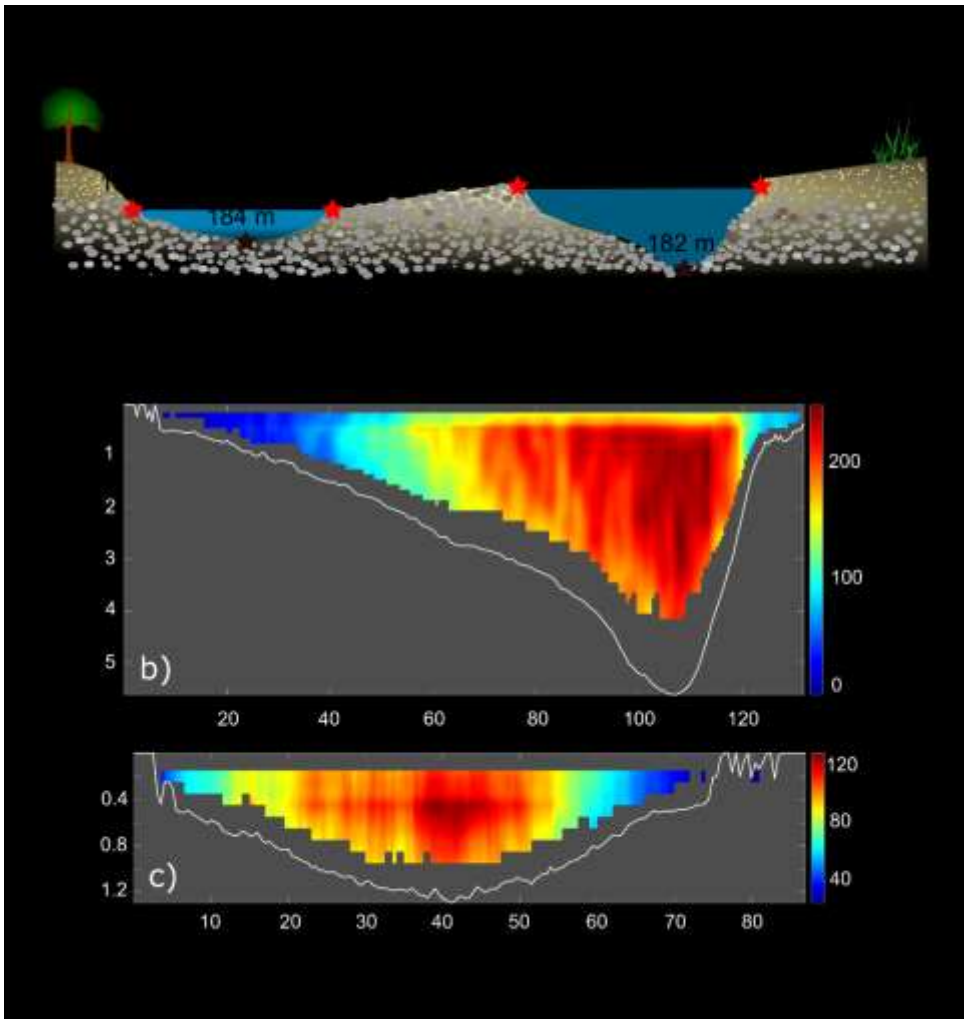

297

Figure 5. Karnali cross-sections downstream of bifurcation, looking downstream. a) Schematic cross-section showing the difference in absolute bed and bank elevation between the west and east branches immediately downstream of the main bifurcation node, based on ADCP transects in October 2016 (shown in b and c). b) ADCP transect from the main channel (west branch) showing channel depth and flow velocity. c) ADCP transect from the secondary channel (east branch). Both ADCP transects have been processed using the Velocity Mapping Toolbox (VMT) v4.09 (Parsons et al., 2013).

3.2 Modelling results

The 1D HEC-RAS model using the SRTM DEM was developed by the Nepal Department of Hydrology and Meteorology (DHM) by extracting multiple topographic cross-sections at critical locations perpendicular to the Karnali river channel (personal communication, October 2019), including at the bridges and the bifurcation point (Figure 1), and interpolating the results between cross-sections. The difference in inundation extent between the 1D HEC-RAS model results and the 2D Delft3D model, visually represented in Figure 4a and 4b, is likely due to the spatial resolution and the selection of cross-section data in the HEC-RAS model. For example, generally, the west branch river channel is deeper in the Delft 3D model (Figure 4b) than the HEC-RAS model (Figure 4a), and less water is observed on the western floodplain, near Tikapur in the Delft3D model (see Figure 4). The 2D Delft3D model may represent the channel geometry more accurately, thus increasing the channel capacity and containing the flow in this location for the given discharge.

Changing the DEM resolution and age (from SRTM to TanDEM-X) within the Delft3D model resulted in a 9.5% increase in flood inundation extent for depths greater than 0.5 m (Figure 4b and 4c; Table 1). Visually, the smaller secondary channels or braid

channels north of the town of Tikapur (Figure 4c) are better represented by the higher spatial resolution of the TanDEM-X data. The depth in the east branch of the river is larger in the SRTM DEM compared to the TanDEM-X DEM, suggesting a greater percentage of the flow is routed down the east branch. The east bank of the east branch is characterised by a 5-10 m high alluvial terrace with dense tree cover provided by the Bardia National Park. Consequently, when more flow is diverted down the east branch in Figure 4b, the flood is contained by the higher bank elevation, reflected by higher water depth within the channel (i.e. yellow pixels). This causes slightly increased flooding in the central floodplain area, along the west bank of the east branch of the river, and decreased flooding along the banks of the western branch. Resampling the TanDEM-X to a coarser resolution 30 m DEM resulted in a 1% decrease in inundation area (Figure 4d). In Figure 4d, the distribution of flow down the two branches is similar to that for the 10 m TanDEM-X (Figure 4c), and the depth in the east branch is smaller for the 30 m TanDEM-X than for the 30 m SRTM (Figure 4b). Flood inundation maps for depths > 0.05 m, included in the supplementary material, follow these trends.

When the bed elevation is reduced in Scenario 2, overall flooding extent is reduced by ~36% (Table 1), as seen by comparing Figure 6a with Figure 6b. Lastly, when the bed elevation is reduced and the bifurcation bed levels are changed in Scenario 3 to integrate the bed levels observed in the field in October 2016 (Figure 6c), more flooding is observed than in Scenario 2 (-32% compared to -36%, Table 1), particularly in the west floodplain.

342 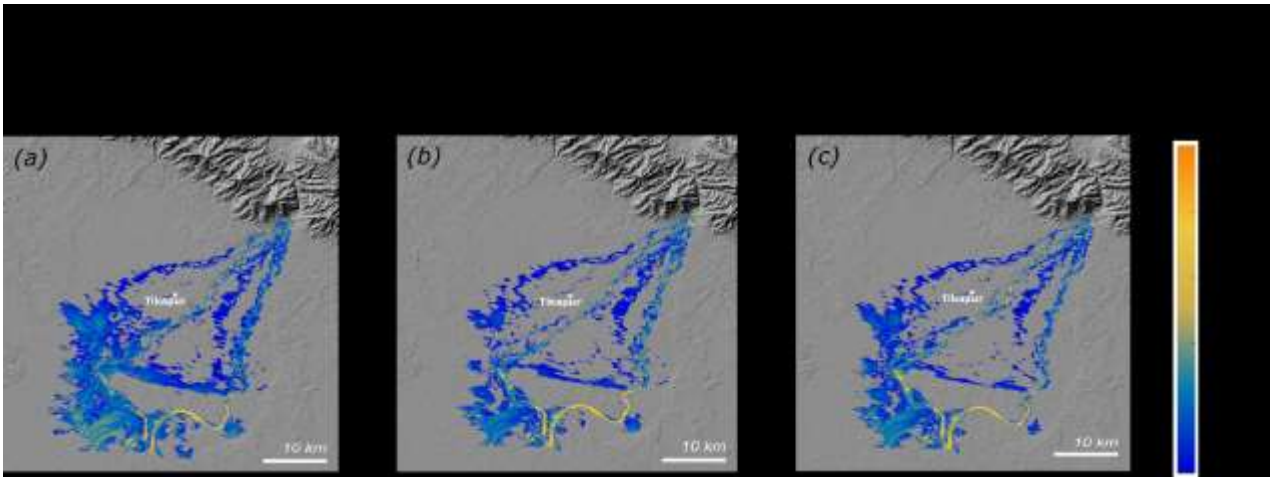

343 *Figure 6. Inundation extent and depth (> 0.5 m) for a 1 in 20 yr flood discharge for a) Scenario 1, DEM*
344 *unmodified, bed elevation given by surface water level in the DEM; b) Scenario 2, where bed elevation is*
345 *reduced by 1.8 m; c) Scenario 3, where bed elevation is reduced by 1.8 m, except at the bifurcation where*
346 *the bed is reduced by 5 m in the west branch and 0.5 m in the east branch.*

347

348 Reducing the bed elevation uniformly from Scenario 1 to 2 results in a 36% decrease in
349 inundation area (Table 1), and a notable decrease in flood extent in the western floodplain
350 (Figure 6b). When the bifurcation is then modified (Scenario 3, Figure 6c), slightly more
351 flooding is observed in the western floodplain but flood extent is reduced in the central
352 floodplain that separates the two branches, when comparing to Scenario 2 (Figure 6b). In
353 Scenario 2, the east branch is the major river branch conveying the majority of the flow
354 (Figure 7b). Similarly to the SRTM DEM (Figure 4b), when more flow is diverted down the
355 east branch in Figure 6b, the flood is contained by the higher bank elevation, reflected in
356 the higher water depths within the channel. This results in slightly increased flooding on
357 the banks of the eastern branch and decreased flooding along the banks of the western
358 branch.

Figure 7 presents discharge hydrographs in the east and west branches for Scenarios 1, 2 and 3, for Delft3D models using the 10 m TanDEM-X data, for the 20-year flood discharge. When the DEM is unchanged, the flow is evenly distributed down the west and east branches, with slightly more flow (approximately 55-60%) in the west branch. When the bed elevation is uniformly reduced by 1.8 m (Figure 7b), the east branch becomes the main channel, accounting for between 75-90% of discharge before the peak flood arrives, and 60% at peak flood discharge. The biggest change in flow distribution is observed when the DEM is modified and the bed elevation at the bifurcation is updated to reflect the October 2016 field observations. In Figure 7c, approximately 85-90% of flow goes down the west branch before the peak flood, and approximately 65% at peak flood flow. Before the peak flood arrives (beginning at ~34 days, Figure 7c), the discharge ratio is similar to the field observations from October 2016 (Figure 1).

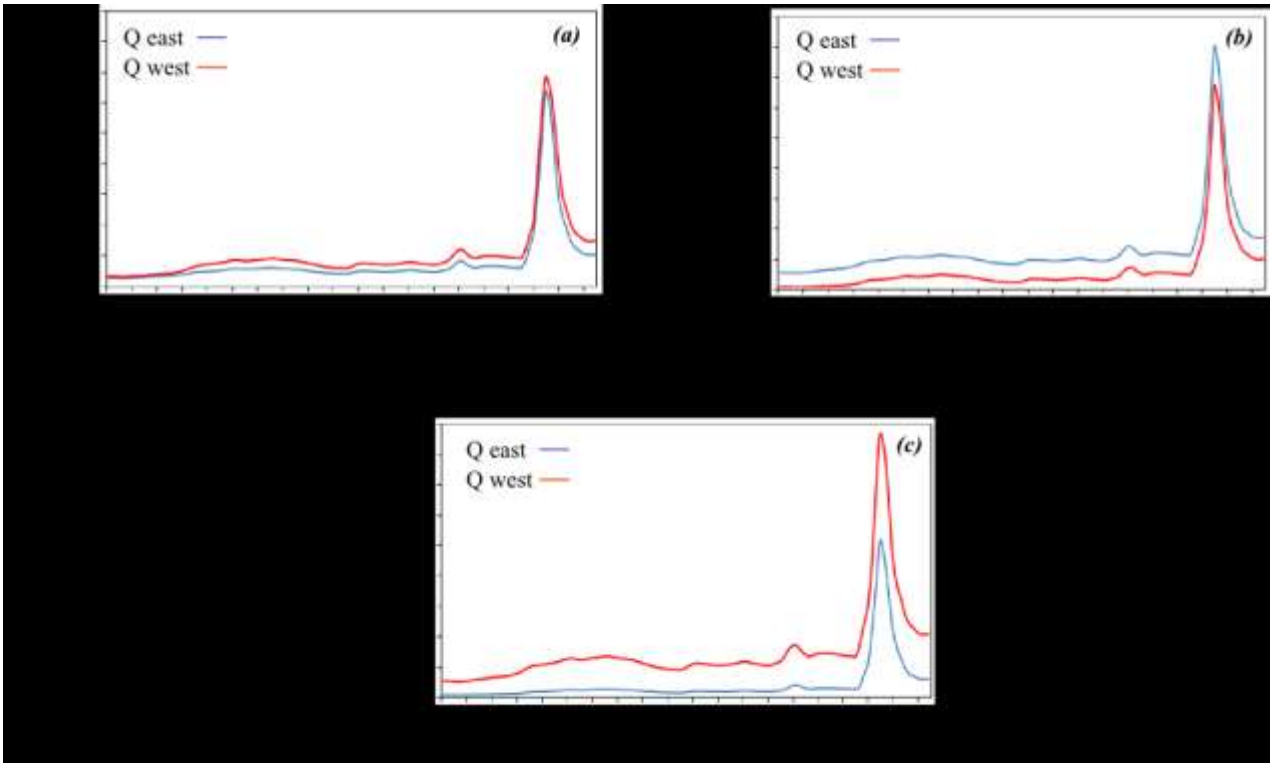

372

373 *Figure 7. Modelled hydrographs for the 20-year flood, in the east and west branches for a) Scenario 1*
374 *(baseline, no change to DEM), b) Scenario 2 (uniformly lowered bed) and c) Scenario 3 (uniformly lowered*
375 *bed and bifurcation modified).*

376

377 *Table 1: Percentage change in the inundation extent between scenarios and model configurations (area km^2)*

	Scenario 1 (unmodified TanDEM-X DEM)	***Scenario 2 (uniformly lowered bed)***	***Scenario 3 (bifurcation modification)***	***Scenario 4 (resampled DEM)***	***SRTM DEM***	***SRTM DEM with 1D HEC-RAS model***
% change in area for inundation depths > 0.5 m	*Baseline (320 km^2)*	*-36%*	*-32 %*	*-0.9%*	*-9.5%*	*-20.5%*

378

4. Discussion

The reduction in flood inundation area between Scenario 1 (baseline scenario with channel depth defined by the surface water level in DEM) and Scenario 2 (uniformly lowered bed) is indicative of how flood inundation patterns may respond to episodes of extreme channel incision, such as might be expected following large storms. In the opposite scenario (i.e., where a channel evolves from Scenario 2 to Scenario 1), such as might be expected following periods of enhanced sediment delivery into the foreland basin (e.g. earthquake-induced landslide inputs), there may be several meters of bed aggradation, resulting in a large increase in inundation extent (e.g. Keefer,1999; Chen and Petley, 2005). Scenario 3 used the bed elevations of Scenario 2, but modified river bed elevations at the bifurcation area to represent elevations observed in the field in October 2016. Changing bed elevations in this small region of the river increased downstream flood extent (-32% compared to -36%, Table 1), with new areas predicted to experience flow depths > 0.5 m (Figures 6b, 6c). As a result of the elevation changes at the bifurcation, the main or dominant river channel (with the greater discharge) switched from the east to the west between Scenario 2 and Scenario 3 (Figure 7b & c). The modelled hydrographs of Scenario 3, shown in Figure 7c, represent most accurately the discharge distribution observed in October 2016 (Figure 1).

The increase in inundation extent associated with the change in DEM (from SRTM to TanDEM-X in Figure 4b and 4c) may also relate to improved representation of the channel geometry and the braided channel network. In the coarser SRTM DEM, only channels or braids with widths greater than two pixels (> 60 m) are likely to be captured in the DEM. With the higher resolution TanDEM-X DEM, the channel network in the upper

portion of the system is better represented, especially where the flow geometry is characterised by much narrower (< 60 m) and multiple channel braids than the downstream portion. Improved representation of these smaller secondary channel networks allows flow to reach adjacent regions of the floodplain in the model more easily than the topographic conditions represented by the SRTM DEM. This results in an increase in the number of wet cells and hence inundation extent for the same flood discharge. The relatively small change (<1 %) in inundation extent between the 10 m TanDEM-X and resampled 30 m TanDEM-X DEMs, in comparison to the change from the older 30 m SRTM to the newer unmodified 2013 TanDEM-X DEM (9.5%), suggests that reduced vertical error and improved representation of the current channel configuration are likely to have greater impact on flood inundation modelling than simply improving the horizontal resolution of the DEM. In river systems as dynamic as the Karnali River, accurate representation of channel configuration and elevation is a prerequisite for improved flood inundation modelling.

Given the highly variable seasonal discharge and large sediment loads exported by rivers into the Ganga Plain (e.g. Tandon et al., 2006), variable bed elevation and high channel migration rates are key geomorphological features of these systems which need to be incorporated into predictive flood hazard modelling. The results presented here demonstrate the sensitivity of modelled flood inundation extents to 1) sediment driven changes in bed elevation and 2) the temporal variability in channel position based on two DEMs captured 12 years apart. Our results highlight the role that these processes play in modelled flood inundation extent, and that geomorphological processes need to be incorporated to improve future flood hazard prediction.

4.1 Limitations

A combination of large sediment loads, poorly consolidated and unvegetated channel banks, and peaked seasonal hydrographs contribute to the development of highly dynamic and mobile river channels across low relief landscapes, such as those downstream of the Himalayan mountains. Large storms or sediment generating events (e.g. widespread earthquake-induced landsliding) also drive aggradation in the downstream alluvial system, which can decrease channel capacity (e.g. Goswami, 1985; Keefer, 1999; Chen and Petley. 2005; Lane et al., 2007; Dingle et al., 2017). In the modelling work presented here, a uniform reduction in bed elevation is assumed between two scenarios (from 1 to 2; Figure 6). Sediment deposition or erosion downstream of the mountain front is unlikely to occur in this spatial fashion. Intuitively, it would be expected that gravel (and coarser) grain sizes will be deposited upstream of the gravel-sand transition, which occurs ~40 - 45 km downstream of Chisapani (Figure 1). If the majority of sediment delivered out of the mountains is sand-sized or finer, this material is expected to remain largely in transport and be deposited on the floodplain (if there is significant overbank flow) or within the channel further downstream of the gravel-sand transition. Deposition of this sediment onto the channel bed is also likely to initiate enhanced lateral migration of sand-bedded channels (e.g. Dingle et al., 2020), as channels can be highly unstable when transporting high sediment loads (e.g. Montgomery et al., 1999). In contrast, rates of vertical incision are likely to be highest closest to the mountain front where channel gradients are greatest. In general, the thickness of sediment deposited or eroded within these types of channels is likely to change with distance downstream in keeping with patterns of subsidence-driven accommodation across a foreland basin (see e.g. Flemings and Jordan, 1989).

448 The changes in bed elevation used in the different scenarios modelled by Delft3D
449 lie within the vertical error or root-mean-square error (RMSE) associated with the SRTM
450 DEM elevations, which vary between ±6.2 and ±22.35 m (Carabajal and Harding, 2006;
451 Rodriguez et al., 2006; Wendi et al., 2016). This highlights the potential error in flood
452 inundation extents modelled using low resolution DEMs of low relief landscapes where
453 small changes or inaccuracies in riverbed elevation can result in significantly under- or
454 over-estimated flood inundation extents. This is further compounded by outdated DEMs,
455 such as the 30 m SRTM DEM (which was captured in 2000), given that mobile channels
456 can migrate 100s to 1000s of m across their floodplains in a single year (e.g. Coleman,
457 1969; Constantine et al., 2014, Dingle et al., 2019). The value of flood inundation models
458 based on outdated topographic data in these types of morphologically active regions is
459 questionable. In comparison, the RMSE of the TanDEM-X DEM is considerably lower at
460 ±1.1 to ±1.8 m (Wessel et al., 2018). When the 30 m SRTM data are used, the modelled
461 inundation extent is reduced (Figure 4b), with 9.5% less inundation area than the TanDEM-
462 X model. However, in certain areas of the western floodplain, the depth of the flood is
463 increased in the SRTM model. This could be exacerbated by the error in the SRTM data;
464 overestimated elevations could inhibit the flow, and underestimated elevations could cause
465 accumulation or ponding of flow. The difficulty in validating the numerical models lies in the
466 lack of accurate flood information, which is presently only available in word of mouth form.
467 The orbital interval of satellite imagery is typically several weeks, so is unlikely to capture
468 maximum flood extents. The quality of images is also complicated by increased cloud cover
469 during the monsoon season.

470

4.2 Topographically sensitive points in the channel network

Small changes in channel bed elevation at particularly sensitive points (such as major bifurcation nodes) in the channel network may also have a disproportionate effect on downstream flow routing and modelled patterns of flood inundation extent (Figure 6). Small changes in absolute bed elevation (relative to the total depth of the channel) at the Karnali bifurcation appear to drive changes in flow distribution into the two downstream branches (Figure 7). This is likely to occur through changes in channel gradient, where small amounts of sediment deposition or erosion may alter the gradient advantage down one branch (e.g. Kleinhans et al., 2013). If the branches differ in depth, the amount of water and sediment entering and the sediment transport capacity of each branch are also expected to vary.

Historically, the dominant branch (i.e. carrying the greatest proportion of flow) downstream of the Karnali bifurcation is known to have switched numerous times. While the majority of flow is currently diverted down the west branch, switching of the dominant channel is thought to occur following large floods (Khanal et al., 2016). The last shift in dominant channel from the east to the west branch occurred in 2010 following a large monsoonal flood discharge which had adverse effects on local Ganges river dolphin populations that were forced to relocate into the deeper but more heavily fished western branch (Paudel et al., 2015; Khanal et al., 2016). Landsat satellite imagery captured in November 2001 suggests that the dominant branch was also the west channel at this time, although in a slightly different location to the October 2016 branch (Figure 8). This implies that over the last ~18 years, there have been at least two changes in the dominant channel. Figure 8 suggests that changes in bed elevation at the Karnali river bifurcation, due to

deposition and aggradation, lead to a switch in the dominant river channel, during both low and peak flow seasons. As the dominant channel changes, existing flood inundation models will have significantly reduced value, as they will likely under-estimate inundation extent in the region surrounding the new dominant channel and over-estimate in the area where the dominant channel was originally located (Figure 6b). In general, the most mobile parts of the river system are situated downstream of the gravel-sand transition, where rates of lateral channel migration may be several hundred meters over a single year (Dingle et al., 2020). Given the relative homogeneity of the floodplain, lateral shifting of the channel is likely just to extend the region of inundation in the direction of channel movement. If flow is routed into paleo-channels, these depressions across the landscape may route water further away into regions that were previously unaffected.

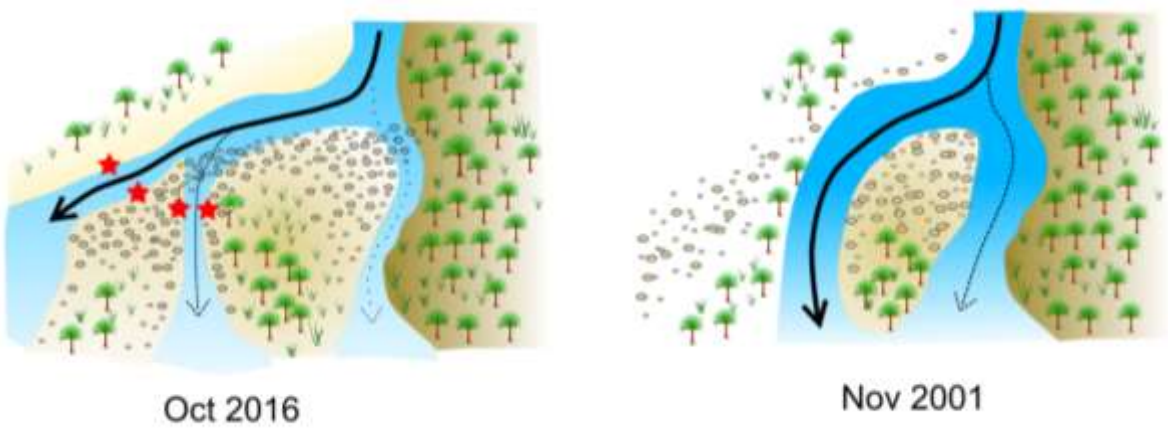

Figure 8. Schematic of Karnali River bifurcation. These images illustrate how the position of the bifurcation has migrated between 2016 and 2001 based on LandSat optical satellite imagery, where both schematics cover identical spatial frames. Solid lines represent the pathway of the main channel conveying the majority

of flow, whilst dotted arrows represented secondary channels. Red stars shown in the October 2016 image correspond to the bank elevations shown in Figure 5a.

In river systems as dynamic as the Karnali, there is a need to constantly update and verify boundary conditions such as channel geometry and the channel boundary positions in order to improve predictive flood inundation models. Simply increasing DEM resolution does not necessarily improve model results dramatically. Capturing the dynamic nature of the fluvial network is especially important in low relief aggrading landscapes that are often characterised by channels with high rates of lateral migration and avulsion. This can be achieved by resurveying the bathymetry and bank elevations following periods of sustained high water and sediment discharges or following channel avulsions. Surveys should be targeted at sensitive points in the landscape, such as the Karnali River bifurcation node, where changes in elevation have the greatest impact on downstream flow routing. Our inundation modelling demonstrates that ~2 m of vertical elevation change can change flood inundation extents by up to ~36%; improving the vertical accuracy of DEMs used in these types of predictive hydrodynamic modelling is key. Ensuring that DEMs are corrected for unrealistic channel depths is also necessary to produce more reliable flood prediction models and flood maps. Our results highlight the need to better understand and represent the physical processes that drive channel switching at topographically sensitive regions of channel networks (e.g. major channel bifurcation points) in such models. For example, how does switching of the dominant channel relate to the ability of a flow to mobilise bed material at these locations (i.e. threshold driven)? Or, is the frequency of channel switching also controlled by factors such as changes in sediment supply or sediment grain size?

533 The next stage of this work will be to develop these models to incorporate dynamic
534 geomorphological processes (e.g., channel avulsion, bed aggradation and degradation,
535 lateral migration) that dominate the dynamics of alluvial river systems downstream of many
536 mountain ranges, not just the Himalaya (e.g. Constantine et al., 2014; Martin-Vide et al.,
537 2014; Dingle et al., 2019). Additional field data will be required to calibrate and validate
538 these more complex flood models, including records of the extent of major flood events
539 and collecting flow discharge, sediment concentration, and river cross section
540 measurements before, during and after the monsoon season.

541

542 5. Conclusions

543 A field-calibrated 2D hydrodynamic flood model (Delft3D) of the Karnali River in west Nepal
544 is presented. Flood inundation extents predicted for a 20-year flood are compared against
545 outputs from an existing 1D HEC-RAS model using both the original 30 m SRTM DEM
546 (captured in 2000) and a new higher resolution (10 m) TanDEM-X DEM, captured in 2013,
547 which more accurately reflects the current channel configuration. A number of scenarios
548 were tested examining changing DEM resolution, variable bed elevation to simulate bed
549 aggradation and incision, and updating bed elevations at a large bifurcation node to reflect
550 field observations. Modest quantities of bed aggradation or incision (relative to the bankfull
551 depth of the channel) were found to significantly modify flood inundation extents across the
552 low relief landscape. Our results suggest that hydrodynamic models of mobile river
553 systems need to be updated with field surveys of channel bathymetry and floodplain
554 topography. Regular field measurements of bed elevation and updated DEMs following
555 large sediment generating events and at topographically sensitive areas, such as large

556 river bifurcations, could help to improve model inputs in future flood prediction models. This
557 is particularly important following large flood events carrying large sediment loads out of
558 mountainous regions, which could lead to bed aggradation and channel switching in alluvial
559 river systems further downstream. A fully integrated morphodynamic model of the Karnali
560 River should be a goal for future studies, as and when high quality fluvial field data become
561 available.

562

563 Acknowledgements

564 This research was funded through a NERC Global Challenges Research Fund Building
565 Resilience grant to H.D.S. (NE/P015905/1) and an EPSRC Global Challenges Research
566 Fund Institutional Sponsorship grant (EP/P510944/1) to M.A. German Aerospace Center
567 (DLR) project gourmele_XTI_GLAC0296 provided the TanDEM-X data. The RTK-GPS
568 was loaned from the NERC Geophysical Equipment Facility (loan 1088). We also thank
569 Practical Action Consulting, Laura Quick, Bhairab Sitaula and Nirajan Rayamajhee for
570 assistance in the field and the Nepalese Department of Hydrology and Meteorology for the
571 provision of discharge data.

572

573 References

574 Aalto, R., Maurice-Bourgoin, L., Dunne, T., Montgomery, D.R., Nittrouer, C.A. and Guyot,
575 J.L., 2003. Episodic sediment accumulation on Amazonian floodplains influenced by El
576 Nino/Southern Oscillation. *Nature*, *425*(6957), p.493.

577

578 Carabajal, C.C. and Harding, D.J., 2006. SRTM C-band and ICESat laser altimetry
579 elevation comparisons as a function of tree cover and relief. *Photogrammetric Engineering*
580 *& Remote Sensing*, *72*(3), pp.287-298.

581

582 Chadwick, A., Morfett J., Borthwick M. *Hydraulics in civil and environmental engineering,*
583 *fourth edition*. Spon, 2004.

584

585 Chakraborty, T., Kar, R., Ghosh, P. and Basu, S., 2010. Kosi megafan: Historical records,
586 geomorphology and the recent avulsion of the Kosi River. *Quaternary International*, *227*(2),
587 pp.143-160.

588

589 Chen, H. and Petley, D.N., 2005. The impact of landslides and debris flows triggered by
590 Typhoon Mindulle in Taiwan. *Quarterly Journal of Engineering Geology and Hydrogeology*,
591 *38*(3), pp.301-304.

592

593 Coleman, J.M., 1969. Brahmaputra River: channel processes and sedimentation.
594 *Sedimentary geology*, *3*(2-3), pp.129-239.

595

596 Constantine, J.A., Dunne, T., Ahmed, J., Legleiter, C. and Lazarus, E.D., 2014. Sediment
597 supply as a driver of river meandering and floodplain evolution in the Amazon Basin. *Nature*
598 *Geoscience*, *7*(12), p.899.

599

600 Dehecq, A., Millan, R., Berthier, E., Gourmelen, N., Trouvé, E. and Vionnet, V., 2016.
601 Elevation changes inferred from TanDEM-X data over the Mont-Blanc area: Impact of the
602 X-band interferometric bias. *IEEE Journal of Selected Topics in Applied Earth*
603 *Observations and Remote Sensing*, *9*(8), pp.3870-3882.

604

605 Dingle, E.H., Sinclair, H.D., Attal, M., Milodowski, D.T. and Singh, V., 2016. Subsidence
606 control on river morphology and grain size in the Ganga Plain. *American Journal of*
607 *Science*, *316*(8), pp.778-812.

608

609 Dingle, E.H., Attal, M. and Sinclair, H.D., 2017. Abrasion-set limits on Himalayan gravel
610 flux. *Nature*, *544*(7651), p.471.

611

612 Dingle, E.H., Paringit, E.C., Tolentino, P.L., Williams, R.D., Hoey, T.B., Barrett, B., Long,
613 H., Smiley, C. and Stott, E., 2019. Decadal-scale morphological adjustment of a lowland
614 tropical river. *Geomorphology*, *333*, pp.30-42.

615

616 Dingle, E.H., Sinclair, H.D., Venditti, J, Attal, M., Kinnaird, T.C., Creed, M., Quick, L.,
617 Nittrouer, J.A. and Gautam, D., 2020. Sediment dynamics across gravel-sand transitions:
618 Implications for river stability and floodplain recycling. *Geology, Vol. 48*

619

620 Eineder, M., Jaber, W.A., Floricioiu, D., Rott, H. and Yague-Martinez, N., 2011, July.
621 Glacier flow and topography measurements with TerraSar-X and TanDEM-X. In *2011 IEEE*
622 *International Geoscience and Remote Sensing Symposium* (pp. 3835-3838). IEEE.

623

624 Flemings, P.B. and Jordan, T.E., 1989. A synthetic stratigraphic model of foreland basin
625 development. *Journal of Geophysical Research: Solid Earth*, *94*(B4), pp.3851-3866.

626

627 Goswami, D.C., 1985. Brahmaputra River, Assam, India: Physiography, basin denudation,
628 and channel aggradation. *Water Resources Research*, *21*(7), pp.959-978.

629

630 Grieve, S.W., Mudd, S.M., Milodowski, D.T., Clubb, F.J. and Furbish, D.J., 2016. How does
631 grid-resolution modulate the topographic expression of geomorphic processes? *Earth*
632 *Surface Dynamics*, *4*(3), p.627.

633

634 Keefer, D.K., 1999. Earthquake-induced landslides and their effects on alluvial fans.
635 *Journal of Sedimentary Research*, *69*(1), pp.84-104.

636

637 Khanal, G., Suryawanshi, K.R., Awasthi, K.D., Dhakal, M., Subedi, N., Nath, D., Kandel,
638 R.C. and Kelkar, N., 2016. Irrigation demands aggravate fishing threats to river dolphins in
639 Nepal. *Biological conservation*, *204*, pp.386-393.

640

641 Kleinhans, M.G., Ferguson, R.I., Lane, S.N. and Hardy, R.J., 2013. Splitting rivers at their
642 seams: bifurcations and avulsion. *Earth Surface Processes and Landforms*, *38*(1), pp.47-
643 61.

644

645 Krieger, G., Moreira, A., Fiedler, H., Hajnsek, I., Werner, M., Younis, M. and Zink, M., 2007.
646 TanDEM-X: A satellite formation for high-resolution SAR interferometry. *IEEE*
647 *Transactions on Geoscience and Remote Sensing*, *45*(11), pp.3317-3341.

648

649 Lane, S.N., Tayefi, V., Reid, S.C., Yu, D. and Hardy, R.J., 2007. Interactions between
650 sediment delivery, channel change, climate change and flood risk in a temperate upland
651 environment. *Earth Surface Processes and Landforms: The Journal of the British*
652 *Geomorphological Research Group*, *32*(3), pp.429-446.

653

654 Lupker, M., Blard, P.H., Lavé, J., France-Lanord, C., Leanni, L., Puchol, N., Charreau, J.
655 and Bourlès, D., 2012. 10 Be-derived Himalayan denudation rates and sediment budgets
656 in the Ganga basin. *Earth and Planetary Science Letters*, *333*, pp.146-156.

657

658 Martín-Vide, J.P., Amarilla, M. and Zárate, F.J., 2014. Collapse of the Pilcomayo River.
659 *Geomorphology*, *205*, pp.155-163.

660

661 Montgomery, D.R., Panfil, M.S. and Hayes, S.K., 1999. Channel-bed mobility response to
662 extreme sediment loading at Mount Pinatubo. *Geology*, *27*(3), pp.271-274.

663

664 Parsons, D.R., Jackson, P.R., Czuba, J.A., Engel, F.L., Rhoads, B.L., Oberg, K.A., Best,
665 J.L., Mueller, D.S., Johnson, K.K., and Riley, J.D., 2013, Velocity Mapping Toolbox (VMT):
666 a processing and visualization suite for moving-vessel ADCP measurements. *Earth*
667 *Surface Processes and Landforms*, 38, pp. 1244–1260.

668

669 Paudel, S., Timilsina, Y.P., Lewis, J., Ingersoll, T. and Jnawali, S.R., 2015. Population
670 status and habitat occupancy of endangered river dolphins in the Karnali River system of
671 Nepal during low water season. *Marine Mammal Science*, *31*(2), pp.707-719.

672

673 Pelletier, J.D., 2013. A robust, two-parameter method for the extraction of drainage
674 networks from high-resolution digital elevation models (DEMs): Evaluation using synthetic
675 and real-world DEMs. *Water Resources Research*, *49*(1), pp.75-89.

676

677 Quick, L., Sinclair, H.D., Attal, M. and Singh, V., 2019. Conglomerate recycling in the
678 Himalayan foreland basin: Implications for grain size and provenance. *Geological Society*
679 *of America Bulletin*.

680 Rana, N., Singh, S., Sundriyal, Y.P. and Juyal, N., 2013. Recent and past floods in the
681 Alaknanda valley: causes and consequences. *Current Science*, *105*(9), pp.1209-1212.

682

683 Risk Nexus, 2015 (post event review capability report): *Urgent case for recovery: what we*
684 *can learn from the August 2014 Karnali River floods in Nepal*. Written by Institute for Social
685 and Environmental Transition (ISET International and ISET-Nepal), Practical Action Nepal
686 and the Zurich Insurance Company.

687

688 Rodriguez, E., Morris, C.S. and Belz, J.E., 2006. A global assessment of the SRTM
689 performance. *Photogrammetric Engineering & Remote Sensing*, *72*(3), pp.249-260.

690

691 Sinha, R. and Friend, P.F., 1994. River systems and their sediment flux, Indo-Gangetic
692 plains, Northern Bihar, India. *Sedimentology*, *41*(4), pp.825-845.

693

694 Sinha, R., Jain, V., Babu, G.P. and Ghosh, S., 2005. Geomorphic characterization and
695 diversity of the fluvial systems of the Gangetic Plains. *Geomorphology*, *70*(3-4), pp.207-
696 225.

697

698 Sinha, R., 2009. The great avulsion of Kosi on 18 August 2008. *Current Science*, pp.429-
699 433.

700

701 Sinha, R., Bapalu, G.V., Singh, L.K. and Rath, B., 2008. Flood risk analysis in the Kosi
702 river basin, north Bihar using multi-parametric approach of analytical hierarchy process
703 (AHP). *Journal of the Indian Society of Remote Sensing*, *36*(4), pp.335-349.

704

705 Stover, S. and Montgomery, D.R., 2001. Channel change and flooding, Skokomish River,
706 Washington. *Journal of Hydrology*, 234(3-4), 272-282.

707

708 Slater, L.J., Singer, M.B. and Kirchner, J.W., 2015. Hydrologic versus geomorphic drivers
709 of trends in flood hazard. *Geophysical Research Letters*, *42*(2), pp.370-376.

710

711 Slater, L.J., Khouakhi, A. and Wilby, R.L., 2019. River channel conveyance capacity
712 adjusts to modes of climate variability. *Scientific reports*, *9*(1), pp.1-10.

713

714 Tandon, S.K., Gibling, M.R., Sinha, R., Singh, V., Ghazanfari, P., Dasgupta, A., Jain, M.
715 and Jain, V., 2006. Alluvial valleys of the Ganga Plains, India: Timing and causes of
716 incision.

717

718 Wendi, D., Liong, S.Y., Sun, Y. and Doan, C.D., 2016. An innovative approach to improve
719 SRTM DEM using multispectral imagery and artificial neural network. *Journal of Advances*
720 *in Modeling Earth Systems*, *8*(2), pp.691-702.

721

722 Wessel, B., Huber, M., Wohlfart, C., Marschalk, U., Kosmann, D. and Roth, A., 2018.
723 Accuracy assessment of the global TanDEM-X Digital Elevation Model with GPS data.
724 *ISPRS Journal of Photogrammetry and Remote Sensing*, *139*, pp.171-182.